

Hybrid collisional-radiative modeling for high-fidelity atomic kinetics

Hybrid collisional-radiative modeling for high-fidelity atomic kinetics

Prashant Sharma,^{1, a)} Christopher J. Fontes,² Mark Zammit,¹ James Colgan,¹ Nathan Garland,^{1, 3, 4} and Xian-Zhu Tang^{1, b)}

¹⁾*Theoretical Division, Los Alamos National Laboratory, Los Alamos, NM 87545*

²⁾*Computational Physics Division, Los Alamos National Laboratory, Los Alamos, NM 87545*

³⁾*Queensland Quantum and Advanced Technologies Research Institute, Griffith University, Nathan, Queensland 4111, Australia*

⁴⁾*School of Environment and Science, Griffith University, Nathan, Queensland 4111, Australia*

The fidelity of collisional-radiative (CR) models is critical for advancing our understanding of radiative properties and ionization balance in fusion plasmas. In this work, we present and evaluate hybrid CR schemes that combine fine-structure resolution with superconfiguration averaging, offering a practical compromise between accuracy and computational efficiency. Two hybrid CR models are developed for helium, lithium, and beryllium, retaining detailed fine-structure states up to selected principal quantum numbers, while higher-lying states are statistically averaged to form superconfigurations. These models are applied to compute radiative power loss, as well as average and effective charge states, across a wide range of electron temperatures and densities. The results are benchmarked against a fully fine-structure-resolved CR model to assess the accuracy of the hybrid approach. The findings demonstrate the versatility of hybrid CR schemes and their suitability for detailed plasma simulations where predictive fidelity must be balanced with computational cost.

^{a)}Electronic mail: phyprashant@gmail.com

^{b)}Electronic mail: xtang@lanl.gov

I. INTRODUCTION

Atomic kinetic models are essential in the accurate modeling of atomic-level populations and their evolution, which is crucial for understanding a wide range of plasma phenomena. These models describe the dynamical behavior of ionic charge states, excited states, and electron distributions under diverse plasma conditions, and effects of various atomic processes such as electron impact excitation and de-excitation, ionization and recombination, radiative decay, etc. in plasma evolution. By linking the microscopic details of atomic collisions in terms of the atomic processes to the overall behavior of the plasma, reliable atomic kinetic models can accurately predict the radiative properties, ionization balance, and plasma transport properties¹. Consequently, such models are indispensable across a broad spectrum of applications, including magnetic fusion^{2,3}, inertial-confinement fusion^{4,5}, astrophysical⁶ and atmospheric plasmas⁷, and laboratory low-temperature plasmas employed in semiconductor processing⁸ and plasma medicine applications⁹.

Traditionally, plasma conditions have been approximated using simpler atomic kinetic models. For high-density, thermally equilibrated plasmas, local thermodynamic equilibrium (LTE) models are generally used, which assume that atomic-level populations follow a Boltzmann distribution at the local temperature, and that non-equilibrium processes can be ignored. At the opposite extreme of very low densities and optically thin plasmas, typical of astrophysical coronae, the coronal-equilibrium (collisional-ionization) approximation is generally used, where the model assumes that spontaneous radiative decay dominates the collisional processes. Although these approximations greatly reduce computational demands, their accuracy is limited to specific conditions, as they can fail in cases with intermediate electron densities, complex ionizing or recombining processes (e.g., charge exchange), or non-Maxwellian electron distributions¹⁰. Additionally, in most laboratory and astrophysical plasmas, neither the coronal equilibrium limit nor the LTE limit strictly applies. In these intermediate regimes, collisional-radiative (CR) models provide a more general description by simultaneously accounting for electron-impact processes, radiative transitions, and finite-density effects. CR models bridge the near-coronal and near-LTE regimes with fewer conceptual limitations than those of simpler approaches. Indeed, in the low-density limit CR models reduce to the coronal approximation, whereas at high densities, they approach the LTE populations.

However, this generality and fidelity come at a significant computational cost. Detailed CR models can become computationally demanding, especially when they include increasingly de-

tailed atomic structure data. For medium- and high- Z elements, the number of electronic configurations and fine-structure (FS) levels grows rapidly, often scaling combinatorially with the principal quantum number n and the total electron occupancy. For example, going from a configuration-average to a fully fine-structure-resolved model can increase the number of coupled levels by one to two orders of magnitude. The resulting rate-equation matrix can easily exceed 10^4 to 10^5 levels for mid- Z ions. Each additional level adds new radiative decay channels, electron-impact excitation and de-excitation processes, autoionization, and recombination rates that must be tracked in a self-consistent manner.

As a result, the rate matrices become extremely large and dense, straining memory and computation time, even when using advanced solvers¹¹. A fully fine-structure CR calculation for a medium- Z plasma may require gigabytes of memory and hours of CPU time. This rapid growth in complexity poses a major bottleneck for detailed modeling of higher- Z plasmas and motivates the search for more computationally efficient approaches that preserve the fidelity of key plasma observables, such as the average charge state, radiative power loss, and charge-state distribution.

To address these computational challenges, we employ a hybrid CR scheme¹² that combines fine-structure resolution with superconfiguration averaging, applied to helium, lithium, and beryllium plasma species. Two variants are developed for this study. The primary model, Hybrid- $(n_{\text{valence}} + 4)$, retains all states up to $n_{\text{valence}} + 4$ with full fine-structure resolution while statistically averaging higher states (up to $n = 10$), and a reduced version, Hybrid- (n_{valence}) , is constructed to examine the convergence behavior. Here, n_{valence} denotes the principal quantum number of the highest occupied shell in the ground state of the atom or ion. A key distinction of our approach is that it begins with a fully fine-structure level set and associated atomic data, systematically grouping only the higher-lying states into superconfigurations. This strategy significantly reduces the number of levels and transitions, improving computational efficiency while preserving essential atomic structure details. The hybrid framework also provides a more general basis since collisional and radiative rates are computed directly from fine-structure-resolved cross-sections and rates rather than from pre-averaged quantities. Here we benchmark the hybrid model performance against fully fine-structure-resolved CR models for the same species under steady-state conditions, assessing the radiative power loss, average charge state, and effective charge state across a wide range of electron temperatures and electron densities.

II. COLLISIONAL-RADIATIVE MODEL

The CR model describes the time evolution of atomic state populations through a set of coupled rate equations that account for all processes connecting different levels,

$$\frac{dN_i}{dt} = \sum_{j \neq i} N_j R_{j \rightarrow i} - N_i \sum_{j \neq i} R_{i \rightarrow j}, \quad (1)$$

where N_i and N_j are the populations (or number densities) of atomic states i and j , respectively, and $R_{i \rightarrow j}$ denotes the rate for the transition from state i to state j (with the inverse rate $R_{j \rightarrow i}$ defined analogously). These rates include processes such as electron-impact excitation (EIE) and de-excitation (EIDE), spontaneous radiative transitions, electron-impact ionization (EII), three-body recombination (3BR) and radiative recombination (RR), as well as other related processes. The accuracy of these rates depends critically on the quality of the atomic data employed. For a reliable CR model, these data should be benchmarked against high-quality experimental or theoretical reference results to ensure that the relevant atomic physics are accurately represented.

While the time-dependent formulation is crucial for understanding transient plasma behavior, such as that arising from rapid changes in plasma density, temperature, or incident radiation, many practical situations allow for simplifications. Under conditions where the plasma state changes slowly compared to the timescale of population redistribution, a steady-state approximation is often employed. In such regimes, the population distribution becomes time-independent, and the rate equations simplify to

$$\sum_{j \neq i} N_j R_{j \rightarrow i} - N_i \sum_{j \neq i} R_{i \rightarrow j} = 0. \quad (2)$$

Solving the resulting algebraic system of equations allows for solution of atomic kinetics without the added computational cost of the time integration. Such steady-state CR models are routinely used for diagnostic purposes and spectral interpretations, where long-lived or slowly varying conditions prevail.

A. Fusion Collisional-Radiative (FCR) Code

In this work, we employ the FCR code, which has been recently developed to investigate ionization balance and radiative properties over a wide range of plasma conditions, with particular emphasis on regimes relevant to fusion energy applications. It supports multiple refinement levels¹³,

each designed to achieve an optimal balance between computational cost and accuracy. For example, there is fine-structure refinement for low- Z elements, and hybrid or averaged (configuration-average and superconfiguration) approaches for intermediate- and high- Z elements.

A key strength of FCR is its adaptive framework, which selectively incorporates cross-sections and rate coefficients according to their availability. The code preferentially uses cross-section data whenever possible, enabling the treatment of arbitrary electron energy-distribution functions. This feature makes FCR well suited for both Maxwellian core plasmas and non-Maxwellian edge or boundary plasmas, where phenomena such as momentum-space voids^{14–16}, temperature anisotropy¹⁵, bi-Maxwellian distributions¹⁷, and suprathermal electron populations^{18–20} may arise.

For rate calculations, FCR employs an adaptive Gauss–Kronrod quadrature method²¹, which extends the standard Gauss quadrature by adding extra integration points. This approach improves accuracy, particularly for functions with singularities or sharp gradients, without introducing significant computational cost. In the present study, all refinement schemes have been evaluated using a Maxwellian electron distribution function for clarity and consistency.

B. Atomic data calculation and refinement schemes including hybrid scheme

In the present work, the Flexible Atomic Code (FAC)²² is employed to generate a comprehensive set of atomic data, including level energies, oscillator strengths, spontaneous decay rates, and the relevant forward-process cross-sections and rate coefficients (EIE, EII, PI, and AI). These data are systematically incorporated into the FCR code to examine the radiative properties and ionization balance. It is important to note that the EIE cross-sections for neutral targets are calculated using the plane-wave Born (PWB) approximation, whereas the distorted-wave (DW) approximation is employed for ions. In contrast, other processes, including EII, PI, and AI, are treated using the DW method for all charge states, including neutrals.

This selection of methods provides a practical baseline for the present CR modeling and also establishes a flexible foundation for future refinements. In particular, the framework can readily incorporate cross-section scaling procedures for EIE²³ and for EII^{24,25}, which allow neutral-target cross-sections to be refined to more closely reproduce results from non-perturbative approaches such as R-matrix²⁶ and convergent close-coupling²⁷.

However, since the primary objective of this work is to establish and examine the hybrid CR

modeling strategy, the discussion here remains focused on the refinement schemes themselves and their implications for atomic kinetics.

As discussed earlier, the CR models can be composed of states of varying levels of refinement, reflecting a trade-off between accuracy and computational feasibility. At the coarsest level, a superconfiguration CR model¹⁰ groups energy states solely by the principal quantum number (n), providing a compact representation suitable for cases where only low-resolution data are required, or computational resources are limited. A more refined option is the configuration-average CR model^{13,28–30}, which classifies states by both n and the azimuthal quantum number (l), thus capturing more structural detail without the full complexity of resolving every fine-structure level. The fine-structure (J -resolved) model^{13,28,29,31} achieves the highest practical level of refinement by accounting for the coupling of angular momenta associated with the orbital electrons, leading to a total angular momentum J for each atomic energy level.

To highlight the impact of various refinement schemes on key plasma properties, we present a comparison of the radiative power loss for hydrogen at an electron density of 10^{12} cm^{-3} , obtained from superconfiguration, configuration-average, and fine-structure CR models, as shown in Fig. 1. In the present case of hydrogen, it is observed that the configuration-average model yields radiative power losses that are approximately 50% lower than those of the fine-structure model near the peak of the curve. This discrepancy originates from a “state-ordering problem”, i.e. the energy ordering of the fine-structure levels (for example, for $n = 2$: $E_{2p_{1/2}} < E_{2s_{1/2}} < E_{2p_{3/2}}$) cannot be preserved under configuration-averaging (which results, for example, in the following energy order for $n = 2$: $E_{2s} < E_{2p}$). In addition (continuing with the $n = 2$ example for definiteness), the energy location of the $2s_{1/2}$ level in between the $2p_{1/2}$ and $2p_{3/2}$ levels means that the $2s_{1/2}$ level can undergo both excitation and de-excitation processes with the two levels that arise from the $2p$ configuration. This situation introduces an ambiguity when trying to compute the configuration-average rates and cross sections via the configuration-average analog of the superconfiguration expression displayed in Eq. (3) below. In order to address this ambiguity, we choose to exclude the EIE cross-section and radiative decay rate for the $2p_{1/2} \leftrightarrow 2s_{1/2}$ transition when computing the configuration-average quantities. With this choice, the $2s_{1/2}$ level, which has a dipole allowed transition with a lower level in the fine-structure model, becomes the $2s$ metastable, or forbidden, configuration in the configuration-average model, which results in a significant rearrangement of the populations between the two models at low densities. The $2s$ metastable configuration retains a significant amount of population that is not available for dipole emission, thus resulting

in a decrease in the peak of the radiative power loss displayed in Fig. 1. In more complex multi-electron systems, the configuration-averaging can be more complicated than the hydrogenic case in the sense that both resonance and metastable levels can arise from the same configuration. In that case, configuration-average models combine the population of metastable levels with resonance levels that produce dipole radiation, which typically leads to higher, rather than lower, radiative power losses in configuration-average CR models³².

Analogous to the previous discussion for complex multi-electron systems, we note from Fig. 1 that the superconfiguration model shows roughly 30% higher radiative power loss compared with the fine-structure model. This overestimation is due to the grouping of all of the metastable, or forbidden, levels arising from a given Layzer complex³³ with the corresponding resonance levels in that complex. Since the metastable levels can possess a significant amount of population at low plasma densities, grouping them with the resonance levels can artificially increase the emission from dipole allowed transitions. In a fully fine-structure scheme, these metastable levels are treated explicitly and would contribute less to the total radiative power loss. Consequently, while both configuration-average and superconfiguration approaches offer computational advantages over a fine-structure-resolved CR model, they can introduce systematic errors in predicted plasma properties like radiative power loss and average charge state. For example, in this specific case, discrepancies up to 30–50% in the radiative power loss would have dominated the uncertainties in collisional plasma energy transport of a low-temperature boundary plasma. This issue can be a particularly important concern in both: (i) designing plasma power exhaust and divertor detachment solutions for fusion power reactors, and (ii) quantitatively interpreting current experiments. For practical applications like fusion energy, physics fidelity must be considered when choosing an appropriate level of refinement for the CR modeling.

To optimize the balance between completeness and computational tractability, we adopt a hybrid CR modeling strategy that shares the same underlying principle as Hansen et al.¹², though employing a distinctly different methodology. The approach by Hansen et al. begins with a complete set of relativistic configuration-average (RC) states and rates, then selectively replaces a subset of coronal configurations with detailed FS levels, while averaging the remaining RCs into non-relativistic configurations or superconfigurations. This top-down construction ensures completeness, but relies on RC data as the starting point. In contrast, the present work starts from a fully fine-structure-resolved set of levels and systematically aggregates only the highly excited or continuum-like (described below) states into superconfigurations. This bottom-up construction re-

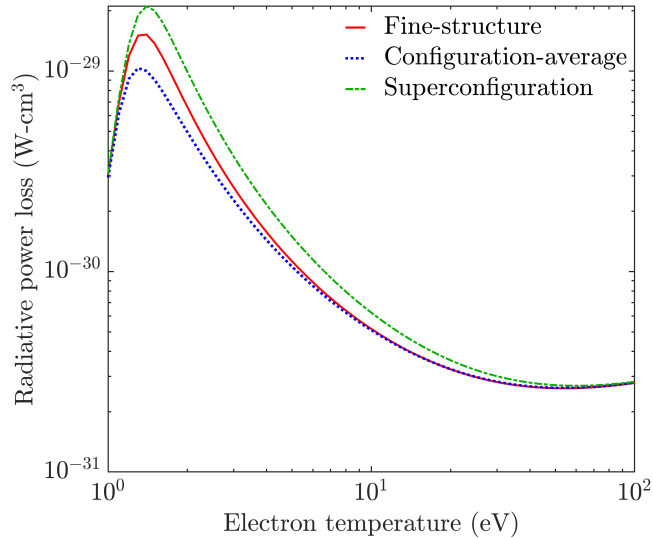


FIG. 1. **Hydrogen:** Comparison of radiative power loss calculated using the superconfiguration (—), configuration-average (···), and fine-structure (—) CR models for $n_e = 10^{12} \text{ cm}^{-3}$. It is noteworthy that the superconfiguration and configuration-average CR models shown here are constructed through statistical averaging of the underlying fine-structure states and the atomic processes connecting them.

tains full FS detail for all low-lying states, which is crucial for describing metastable populations, ladder ionization, and density-sensitive line ratios, while adaptively reducing the state space until convergence of key plasma quantities, such as charge-state distribution and radiative power loss, is achieved.

Figure 2 depicts the underlying concept of the hybrid CR scheme. At lower energies, the key states are fully fine-structure resolved, whereas higher-lying levels are grouped into superconfigurations. The continuum represents the ionization pathways and autoionizing states. Three categories of transitions are indicated as follows:

1. **S–S transitions** connect one superconfiguration to another. These include transitions within singly excited superconfigurations (e.g., (1)(6), (1)(7), (1)(8), etc.) and transitions from singly excited superconfigurations to doubly excited or autoionizing superconfigurations (e.g., (2)², (2)(3), etc.). In the previous sentence, we express superconfigurations in the standard form $(n_1)^{N_1}(n_2)^{N_2} \dots (n_m)^{N_m}$, where n_m represents the principal quantum number of each orbital shell, and N_m specifies the number of electrons occupying the corresponding shell. This notation corresponds to averaging over all configurations that arise from a Layzer

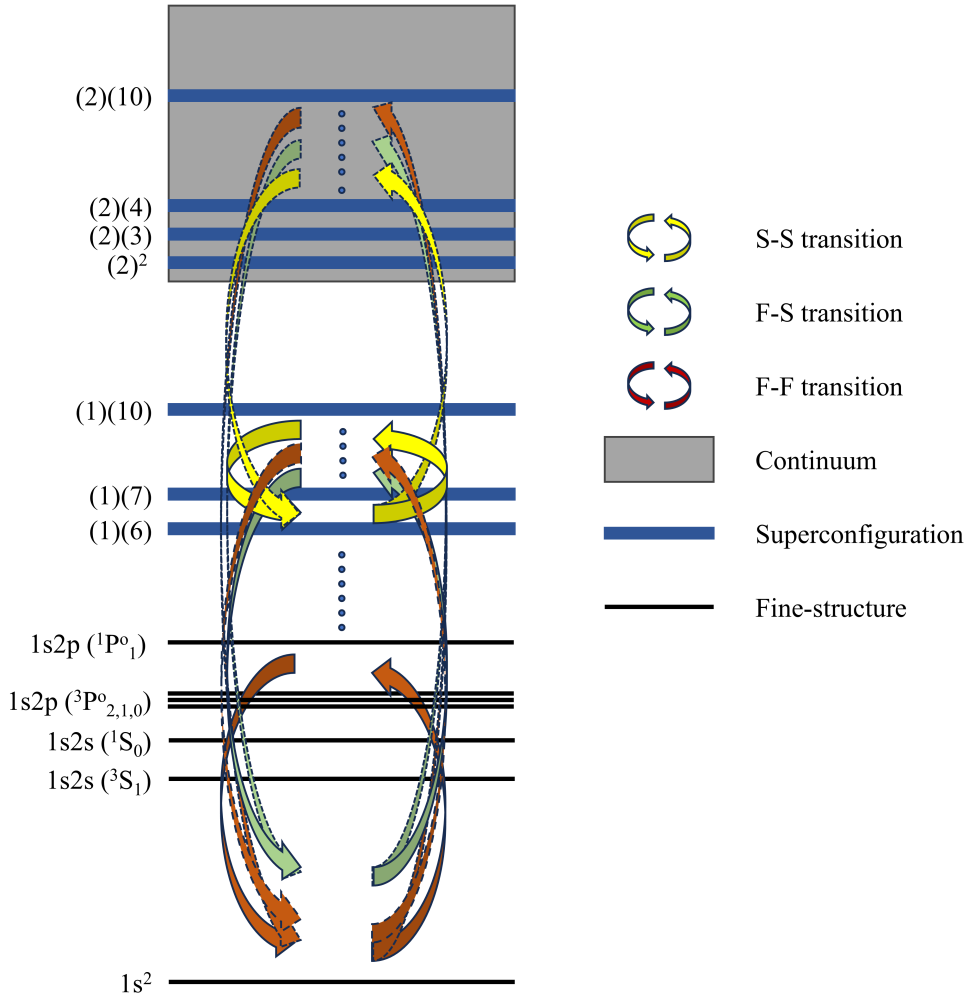


FIG. 2. Schematic of the hybrid scheme for helium (or helium-like ions), showing transitions among fine-structure states, superconfiguration states, and the “handshake” coupling that connects these two regimes. The lower-lying levels are treated with full fine-structure resolution, while higher-lying and continuum-like states are grouped into superconfigurations.

complex³³. If N_m is omitted, it is assumed that $N_m = 1$. Their effective cross-section, σ_{IF}^{SS} , is given by a statistical average over all the individual fine-structure levels $i \in I$ within one superconfiguration I and all levels $f \in F$ in the final superconfiguration F :

$$\sigma_{IF}^{SS} = \sum_{f \in F} \frac{\sum_{i \in I} g_i \sigma_{if}}{\sum_{i \in I} g_i}, \quad (3)$$

where g_i is the statistical weight of the i th level and σ_{if} is the fine-structure cross-section for the $i \rightarrow f$ transition.

2. **F - S transitions** act as a “handshake” between individually resolved fine-structure levels and superconfigurations. These transitions connect the lower resolved levels (e.g., $1s2s(^3S_1, ^1S_0)$, $1s2p(^3P_{2,1,0}^o, ^1P_1^o)$, etc.) to upper superconfiguration blocks (e.g., (1)(6), (1)(7), (2) 2 , (2)(3), etc.). The total cross-section σ_{iF}^{FS} for a fine-structure level i transitioning into a superconfiguration F is obtained by summing σ_{if} over all final states f in F :

$$\sigma_{iF}^{FS} = \sum_{f \in F} \sigma_{if}. \quad (4)$$

3. **F - F transitions** occur completely among fine-structure-resolved levels. Since each fine-structure level is individually retained, one simply uses the direct cross-sections (and rate coefficients) computed for these level-to-level transitions.

As discussed earlier, the cross-sections and rate coefficients of the forward atomic processes, which include EIE, EII, PI, and AI, are taken directly from the fine-structure calculations produced by FAC. The quantities associated with the corresponding inverse processes, namely EIDE, 3BR, RR, and dielectronic recombination, are computed using the detailed balance relation and are applied uniformly across all transition classes (F - F , F - S , and S - S). This procedure ensures that each forward and inverse cross-section or rate-coefficient pair is related through the appropriate statistical weights and Boltzmann factors, thereby maintaining the thermodynamic consistency of the hybrid CR model.

Notably, in the present work, the hybrid scheme is specifically implemented for singly excited states only, while doubly excited states are treated using the superconfiguration approach. For fusion-relevant electron densities, this selective treatment is justified, as the predominantly autoionizing nature of doubly-excited states prevents them from retaining significant population, which makes detailed fine-structure resolution less important than for the low-lying singly-excited states.

This partial-averaging approach, i.e., the hybrid scheme, significantly reduces the number of rate equations as well as the size of the rate matrix that needs to be solved, while still preserving the essential physics. Importantly, the fine-structure levels that play a dominant role in diagnostics and emission spectra remain J -resolved, whereas the superconfiguration approach captures the collective effect of higher-lying states. Hence, the hybrid scheme strikes a balance between accuracy and computational efficiency, enabling detailed CR modeling without requiring full fine-structure resolution across all excited levels.

III. RESULTS AND DISCUSSION

In this work, we have developed two hybrid CR models, Hybrid- $(n_{\text{valence}} + 4)$ and Hybrid- (n_{valence}) , for helium, lithium, and beryllium plasma species. The key distinction between these models lies in the amount of fine-structure resolution that is retained. For example, in the Hybrid- $(n_{\text{valence}} + 4)$ model, fine-structure levels are retained up to $n_{\text{valence}} + 4$, whereas higher-lying states with $n > n_{\text{valence}} + 4$ (up to $n = 10$) are grouped into superconfigurations. In contrast, the Hybrid- (n_{valence}) model applies superconfiguration averaging starting at $n_{\text{valence}} + 1$, offering a more compact representation at the cost of accuracy. A comprehensive list of fine-structure levels and superconfiguration states used in the Hybrid- $(n_{\text{valence}} + 4)$ model for all three elements considered in this work is provided in Table I.

To validate the hybrid scheme, we have benchmarked the hybrid CR models against a fully fine-structure CR model that resolves fine-structure levels up to $n = 10$ for each species. Table II lists the number of levels/states included in the fine-structure and hybrid models, respectively. We then calculated the key plasma properties, including the radiative power loss and average charge state, across electron densities from 10^{12} to 10^{17} cm^{-3} and electron temperatures ranging from 1 to 10^3 eV . The following sections present these comparisons in detail and demonstrate the fidelity of the proposed hybrid CR approach.

TABLE I. Fine-structure levels and superconfigurations for H-like, He-like, Li-like, and Be-like atoms/ions employed in the Hybrid- $(n_{\text{valence}} + 4)$ CR model. Superconfigurations are expressed in the form $(n_1)^{N_1}(n_2)^{N_2} \dots (n_m)^{N_m}$, where n_m represents the principal quantum number of each orbital shell, and N_m specifies the number of electrons occupying the corresponding shell.

Shell	H-like	He-like	Li-like	Be-like
Ground and Singly-excited states				
$n = 1$	$1s ({}^2S_{1/2})$	$1s^2 ({}^1S_0)$	–	–
$n = 2$	$2p ({}^2P_{1/2,3/2}^o)$ $2s ({}^2S_{1/2})$ – –	$1s 2s ({}^3S_1, {}^1S_0)$ $1s 2p ({}^3P_{2,1,0}^o, {}^1P_1^o)$ – –	$1s^2 2s ({}^2S_{1/2})$ – –	$1s^2 2s^2 ({}^1S_0)$ $1s^2 2s 2p ({}^3P_{0,1,2}^o, {}^1P_1^o)$ $1s^2 2p^2 ({}^1D_2, {}^3P_{0,1,2})$ –
$n = 3$	$3p ({}^2P_{1/2,3/2}^o)$ $3s ({}^2S_{1/2})$ $3d ({}^2D_{3/2,5/2}^o)$	$1s 3s ({}^3S_1, {}^1S_0)$ $1s 3p ({}^3P_{0,1,2}^o, {}^1P_1^o)$ $1s 3d ({}^3D_{1,2,3}, {}^1D_2)$	$1s^2 3s ({}^2S_{1/2})$ $1s^2 3p ({}^2P_{1/2,3/2}^o)$ $1s^2 3d ({}^2D_{3/2,5/2}^o)$	$1s^2 2s 3s ({}^3S_1, {}^1S_0)$ $1s^2 2s 3p ({}^3P_{0,1,2}^o, {}^1P_1^o)$ $1s^2 2s 3d ({}^3D_{1,2,3}, {}^1D_2)$
$n = 4$	$4p ({}^2P_{1/2,3/2}^o)$ $4s ({}^2S_{1/2})$ $4d ({}^2D_{3/2,5/2}^o)$ $4f ({}^2F_{5/2,7/2}^o)$	$1s 4s ({}^3S_1, {}^1S_0)$ $1s 4p ({}^3P_{2,1,0}^o, {}^1P_1^o)$ $1s 4d ({}^3D_{1,2,3}, {}^1D_2)$ $1s 4f ({}^3F_{2,3,4}^o, {}^1F_3^o)$	$1s^2 4s ({}^2S_{1/2})$ $1s^2 4p ({}^2P_{1/2,3/2}^o)$ $1s^2 4d ({}^2D_{3/2,5/2}^o)$ $1s^2 4f ({}^2F_{5/2,7/2}^o)$	$1s^2 2s 4s ({}^3S_1, {}^1S_0)$ $1s^2 2s 4p ({}^3P_{0,1,2}^o, {}^1P_1^o)$ $1s^2 2s 4d ({}^3D_{1,2,3}, {}^1D_2)$ $1s^2 2s 4f ({}^3F_{2,3,4}^o, {}^1F_3^o)$
$n = 5$	$5p ({}^2P_{1/2,3/2}^o)$ $5s ({}^2S_{1/2})$ $5d ({}^2D_{3/2,5/2}^o)$ $5f ({}^2F_{5/2,7/2}^o)$ $5f ({}^2G_{7/2,9/2}^o)$	$1s 5s ({}^3S_1, {}^1S_0)$ $1s 5p ({}^3P_{2,1,0}^o, {}^1P_1^o)$ $1s 5d ({}^3D_{3,2,1}, {}^1D_2)$ $1s 5f ({}^3F_{4,3,2}^o, {}^1F_3^o)$ $1s 5g ({}^3G_{5,4,3}, {}^1G_4)$	$1s^2 5s ({}^2S_{1/2})$ $1s^2 5p ({}^2P_{1/2,3/2}^o)$ $1s^2 5d ({}^2D_{3/2,5/2}^o)$ $1s^2 5f ({}^2F_{5/2,7/2}^o)$ $1s^2 5g ({}^2G_{7/2,9/2}^o)$	$1s^2 2s 5s ({}^3S_1, {}^1S_0)$ $1s^2 2s 5p ({}^3P_{0,1,2}^o, {}^1P_1^o)$ $1s^2 2s 5d ({}^3D_{1,2,3}, {}^1D_2)$ $1s^2 2s 5f ({}^3F_{2,3,4}^o, {}^1F_3^o)$ $1s^2 2s 5g ({}^3G_{3,4,5}, {}^1G_4)$

$n = 6$	(6)	(1) (6)	$1s^2 6s (^2S_{1/2})$	$1s^2 2s 6s (^3S_1, ^1S_0)$
	–	–	$1s^2 6p (^2P_{1/2,3/2}^o)$	$1s^2 2s 6p (^3P_{0,1,2}^o, ^1P_1^o)$
	–	–	$1s^2 6d (^2D_{3/2,5/2})$	$1s^2 2s 6d (^3D_{1,2,3}, ^1D_2)$
	–	–	$1s^2 6f (^2F_{5/2,7/2}^o)$	$1s^2 2s 6f (^3F_{2,3,4}^o, ^1F_3^o)$
	–	–	$1s^2 6g (^2G_{7/2,9/2}^o)$	$1s^2 2s 6g (^3G_{3,4,5}, ^1G_4)$
	–	–	$1s^2 6h (^2H_{9/2,11/2}^o)$	$1s^2 2s 6h (^3H_{4,5,6}, ^1H_5^o)$
$n = 7$	(7)	(1) (7)	$(1)^2 (7)$	$(1)^2 (2) (7)$
$n = 8$	(8)	(1) (8)	$(1)^2 (8)$	$(1)^2 (2) (8)$
$n = 9$	(9)	(1) (9)	$(1)^2 (9)$	$(1)^2 (2) (9)$
$n = 10$	(10)	(1) (10)	$(1)^2 (10)$	$(1)^2 (2) (10)$
Doubly-excited states				
$n = 2$	–	$(2)^2$	$(1) (2)^2$	$(1) (2)^3$
$n = 3$	–	$(2) (3)$	$(1) (2) (3)$	$(1) (2)^2 (3), (1)^2 (3)^2$
$n = 4$	–	$(2) (4)$	$(1) (2) (4)$	$(1) (2)^2 (4), (1)^2 (3) (4)$
$n = 5$	–	$(2) (5)$	$(1) (2) (5)$	$(1) (2)^2 (5), (1)^2 (3) (5)$
$n = 6$	–	$(2) (6)$	$(1) (2) (6)$	$(1) (2)^2 (6), (1)^2 (3) (6)$
$n = 7$	–	$(2) (7)$	$(1) (2) (7)$	$(1) (2)^2 (7), (1)^2 (3) (7)$
$n = 8$	–	$(2) (8)$	$(1) (2) (8)$	$(1) (2)^2 (8), (1)^2 (3) (8)$
$n = 9$	–	$(2) (9)$	$(1) (2) (9)$	$(1) (2)^2 (9), (1)^2 (3) (9)$
$n = 10$	–	$(2) (10)$	$(1) (2) (10)$	$(1) (2)^2 (10), (1)^2 (3) (10)$

 TABLE II. Comparison of the number of levels/states in the fine-structure, Hybrid- $(n_{\text{valence}} + 4)$, and Hybrid- (n_{valence}) CR models for different elements.

	Fine-structure	Hybrid- $(n_{\text{valence}} + 4)$	Hybrid- (n_{valence})
Helium	1046	94	30
Lithium	2585	142	50
Beryllium	9790	413	85

A. Helium

Helium plays a central role in fusion plasmas, serving not only as the primary fusion by-product in D–T reactions but also as a commonly employed plasma-conditioning and diagnostic gas in experimental plasma operations. In the context of CR modeling, the recombination and ionization processes are crucially important for helium ash extraction or recycling³⁴ in particular. Its two-electron structure produces rich atomic kinetics with strong electron–electron correlations, singlet–triplet splitting with long-lived metastables, and numerous doubly excited states that autoionize and enable dielectronic recombination.

Figure 3 shows a comparison of the radiative power loss, average charge state, and effective charge state at a fusion-relevant electron density of 10^{14} cm^{-3} , representative of edge and divertor plasma conditions. Both hybrid models follow the fine-structure benchmark over most of the temperature range; however, the Hybrid- (n_{valence}) model shows significant deviations at lower temperatures. In the peak radiative window ranging from 5–50 eV, the Hybrid- $(n_{\text{valence}} + 4)$ model consistently remains within 2% of the fine-structure results for all quantities, whereas the reduced model exhibits errors up to 35% near 3–4 eV. This temperature range corresponds to the transition from neutral to singly ionized helium, where limited level resolution introduces averaging errors in spontaneous radiative decay rates and leads to deviations in the predicted radiative power loss.

At electron temperatures above 20 eV, both hybrid models converge to within 1% of the fine-structure benchmark. This behavior reflects the fact that the plasma is largely ionized in this regime, and the contribution of low-lying fine-structure states to the radiative balance becomes minor.

To further support these findings, we have included parity plots, as shown in Fig. 4, which provide a direct visual comparison between the hybrid predictions and the fine-structure benchmark. In these plots, each point represents a pair of values from the two models, and perfect agreement places the point on the diagonal line. Points clustered near the diagonal indicate that the Hybrid- $(n_{\text{valence}} + 4)$ model successfully reproduces the fine-structure results with high accuracy, while noticeable deviations reveal the limitations of the reduced Hybrid- (n_{valence}) model. These discrepancies become more significant at lower electron densities, where metastable states are not collisionally quenched and can retain larger populations. Their longer lifetimes and density-sensitive transition pathways make the atomic kinetics highly sensitive to level resolution. As the reduced Hybrid- (n_{valence}) model does not fully capture these metastable contributions, it exhibits

larger deviations from the benchmark fine-structure results in this regime.

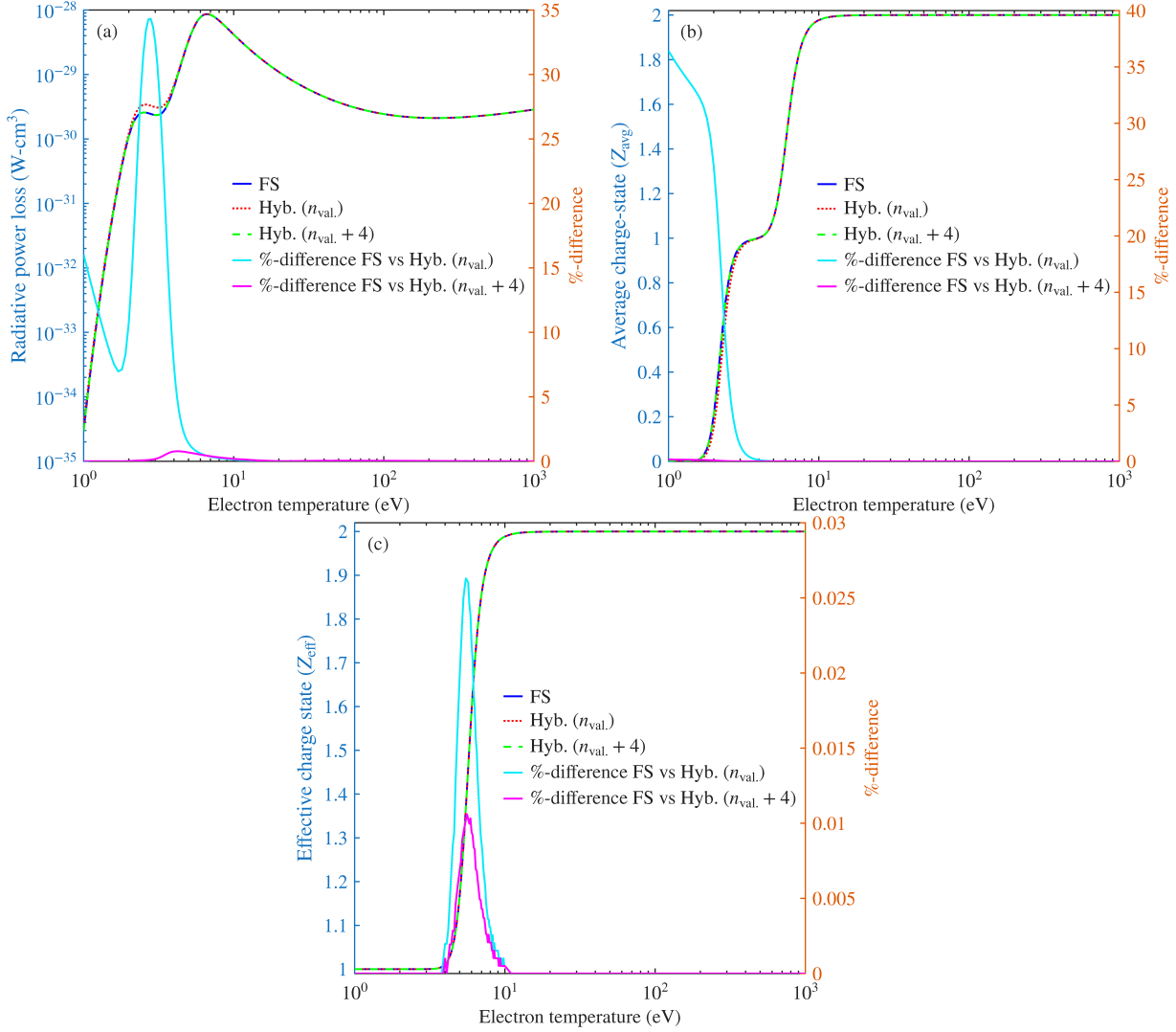


FIG. 3. **Helium:** Comparison of (a) radiative power loss, (b) average charge state, and (c) effective charge state obtained from the fine-structure CR model and two hybrid models, Hybrid- (n_{valence}) and Hybrid- $(n_{\text{valence}} + 4)$, at $n_e = 10^{14} \text{ cm}^{-3}$. The right-hand axes show the percentage deviation of each hybrid model from the fine-structure results. Here, "val." = valence and "Hyb." = Hybrid.

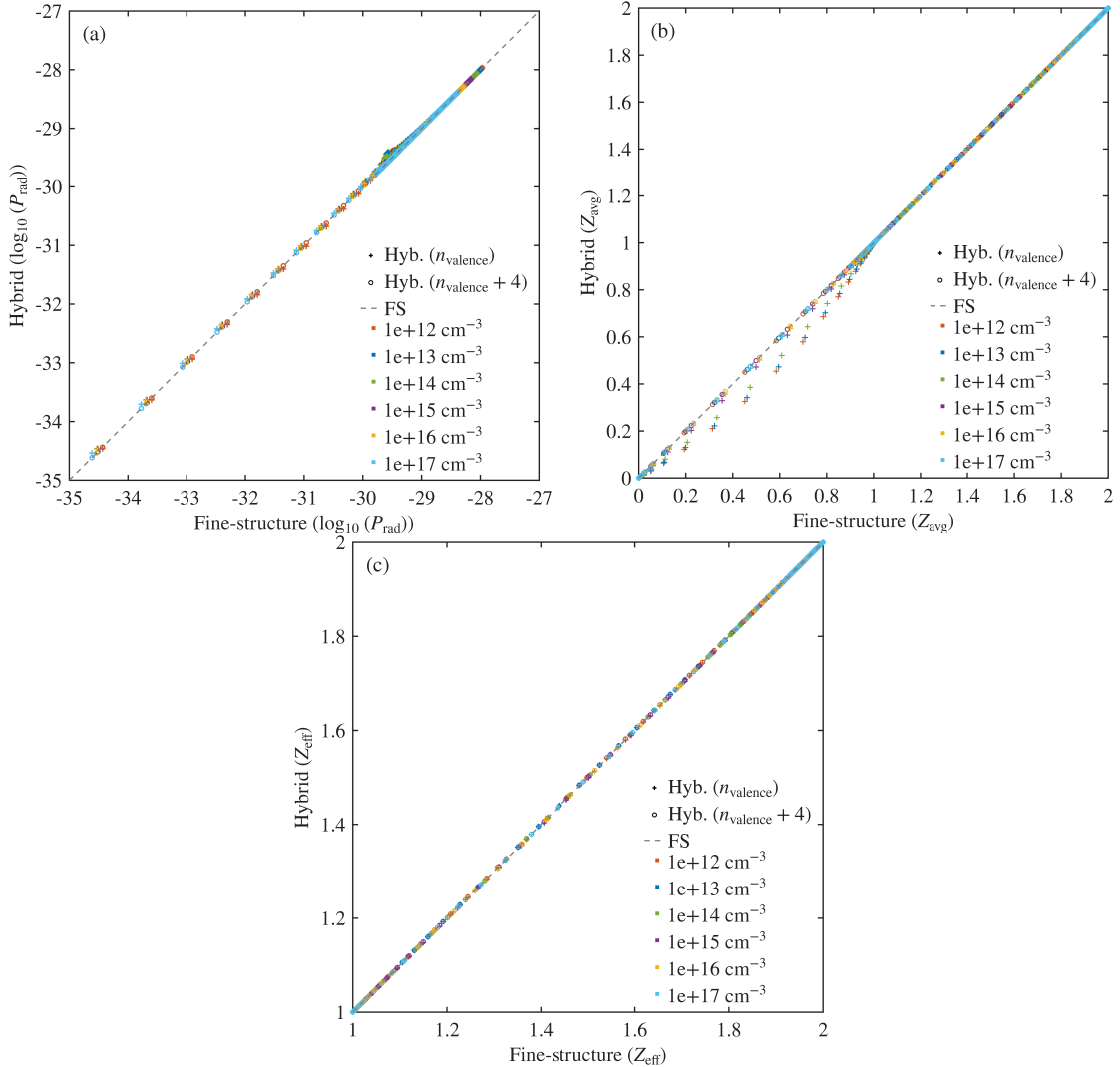


FIG. 4. **Helium:** Parity plots comparing (a) radiative power loss, P_{rad} , (b) average charge state, Z_{avg} , and (c) effective charge state, Z_{eff} , predicted by the Hybrid- (n_{valence}) and Hybrid- $(n_{\text{valence}} + 4)$ models against the fine-structure CR model across electron densities from 10^{12} to 10^{17} cm^{-3} . The dashed diagonal represents perfect agreement ($y = x$); points closer to the line indicate better agreement with the fine-structure benchmark.

B. Lithium

In fusion plasmas, lithium is introduced both as an evaporated wall-conditioning layer³⁵ and as a candidate liquid-metal plasma-facing component³⁶, thereby entering the plasma as a controlled impurity and diagnostic species in many devices. With three electrons, lithium exhibits richer atomic physics than helium: low-lying open-shell structure, numerous doubly excited states, and dense autoionizing and dielectronic recombination resonances provide additional pathways for atomic kinetics and radiation emission.

Figure 5 presents a comprehensive comparison at $n_e = 10^{14} \text{ cm}^{-3}$ for all three key plasma properties, revealing the distinctly different behavior of lithium compared to helium. The radiative power loss exhibits three distinct maxima with a low-temperature peak near $T_e \approx 1 \text{ eV}$ associated with neutral Li line radiation, a sharp dominant peak near $T_e \approx 8 \text{ eV}$ arising from strong Li^+ emission, and a broader maximum around $T_e \approx 25 \text{ eV}$ corresponding to Li^{2+} . This triple-peak structure reflects the sequential ionization of the three electrons of Li. The Hybrid- $(n_{\text{valence}} + 4)$ model captures this complex radiative structure with excellent accuracy, closely reproducing both the sharp primary peak and the broader secondary maximum. The Hybrid- (n_{valence}) model, however, significantly underestimates the secondary radiative peak, demonstrating the critical importance of retaining fine-structure details for higher-lying states in the hybrid treatment.

The ionization balance presents an even more demanding test, exhibiting three well-separated plateaus corresponding to the successive $\text{Li} \rightarrow \text{Li}^+ \rightarrow \text{Li}^{2+} \rightarrow \text{Li}^{3+}$ ionization stages. Each transition occurs over a relatively narrow temperature window, creating sharp increases in the average charge-state curve. The Hybrid- $(n_{\text{valence}} + 4)$ model reproduces these ionization transitions to within 1% accuracy across the full temperature range, capturing both the plateau regions and the sharp transition zones with high fidelity. The reduced hybrid model (n_{valence}), however, systematically underestimates the charge state in the critical 4–20 eV window, where the $\text{Li}^+ \rightarrow \text{Li}^{2+}$ transition dominates the plasma kinetics. This behavior arises from the complex interplay between ionization and recombination processes in the three-electron system, where refinement of singly excited states significantly alters the ionization balance. Further, although both models treat doubly excited states identically, another important consideration is that their different coupling with singly excited states can alter the ionization balance through the competition between autoionization and spontaneous decay from the doubly excited configurations.

The effective charge state exhibits similar structural features at the 4–20 eV electron temper-

ature. The extended hybrid model maintains a robust performance with deviations below 1% throughout this rapidly varying region, whereas the reduced hybrid model shows 30–35% discrepancies.

The parity plots in Fig. 6 provide quantitative confirmation that lithium demands substantially finer resolution than helium to achieve comparable accuracy. While the Hybrid- $(n_{\text{valence}} + 4)$ results maintain a near-diagonal alignment across the full parameter space, the reduced hybrid model exhibits significant scatter, particularly for radiative power-loss predictions. These results establish that for three-electron systems, such as lithium, the extended hybrid approach is essential for reliable plasma modeling.

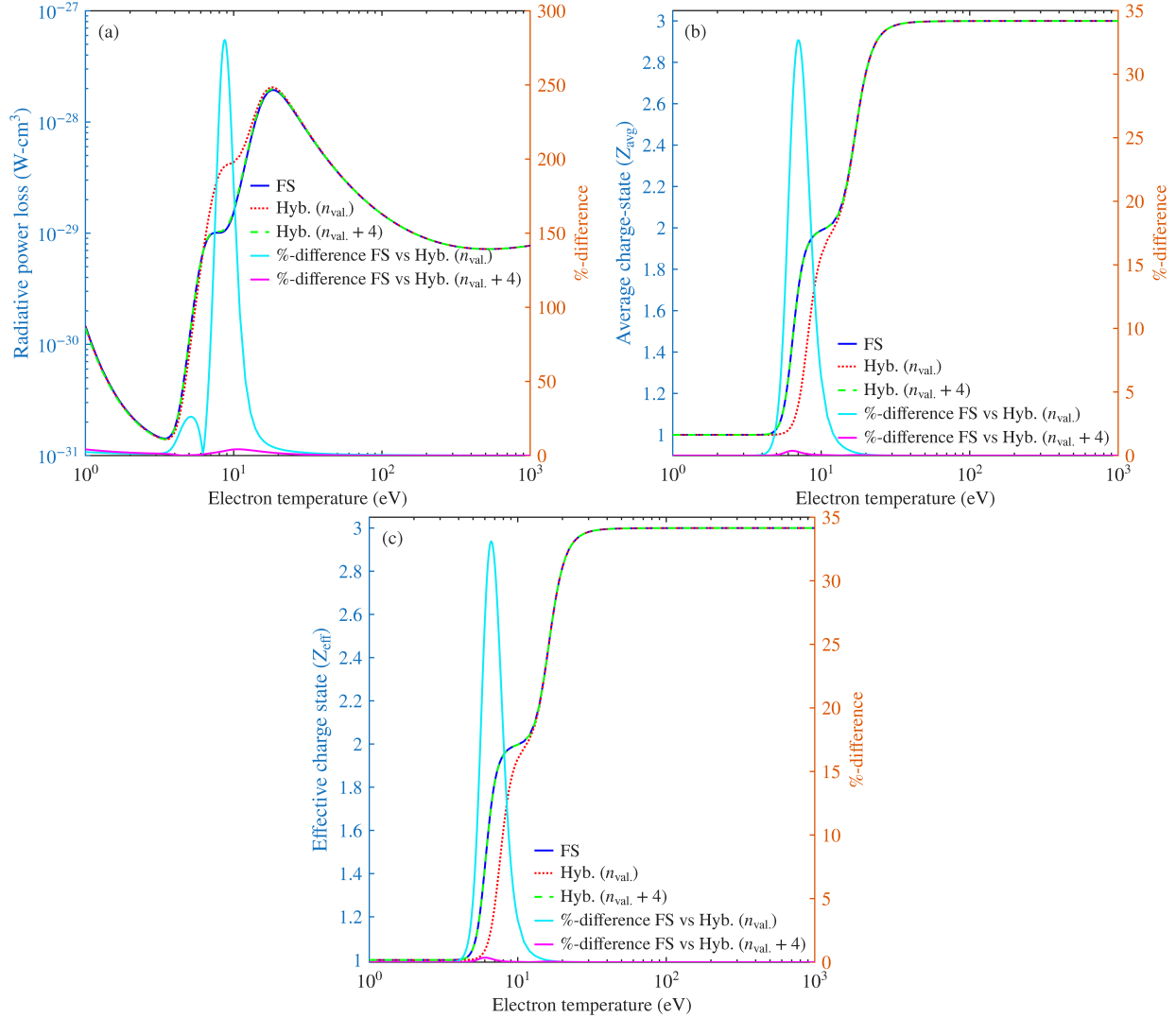


FIG. 5. **Lithium:** Comparison of (a) radiative power loss, (b) average charge state, and (c) effective charge state obtained from the fine-structure CR model and two hybrid models, Hybrid- (n_{valence}) and Hybrid- $(n_{\text{valence}} + 4)$, at $n_e = 10^{14} \text{ cm}^{-3}$. Right-hand axes show the percentage deviation of each hybrid model from the fine-structure results. Here, "val." = valence and "Hyb." = Hybrid.

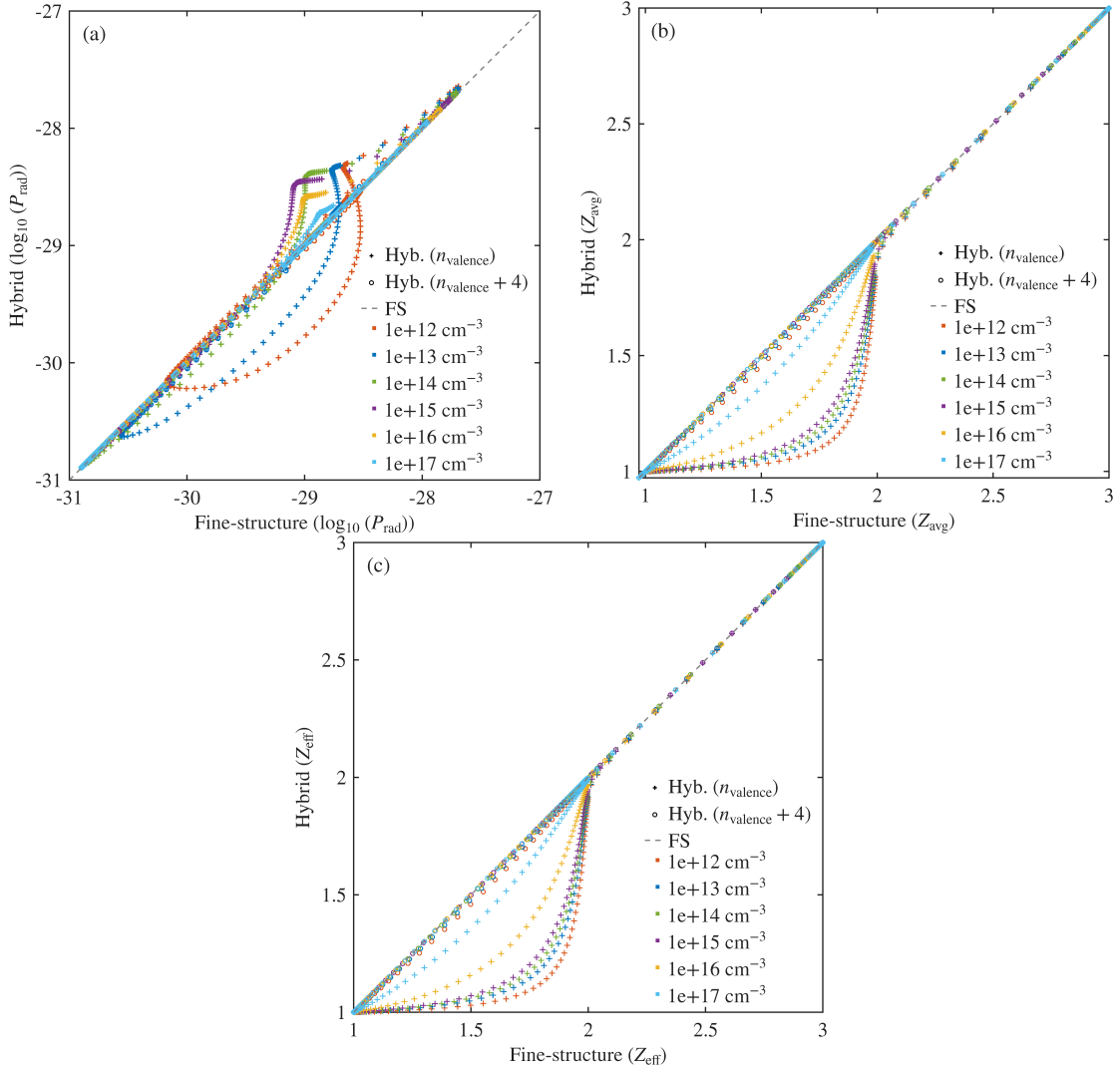


FIG. 6. **Lithium:** Parity plots comparing (a) radiative power loss, P_{rad} , (b) average charge state, Z_{avg} , and (c) effective charge state, Z_{eff} , predicted by Hybrid- (n_{valence}) and Hybrid- $(n_{\text{valence}} + 4)$ models against the fine-structure CR model across electron densities from 10^{12} to 10^{17} cm^{-3} . The dashed diagonal represents perfect agreement ($y = x$); points closer to the line indicate better agreement with the fine-structure benchmark.

C. Beryllium

Beryllium is another useful benchmark for fusion plasmas as it has been a plasma-facing material on the ITER-like first wall on JET³⁷ and thus an important impurity that must be understood for interpreting JET plasma scenarios. Although the updated design of ITER has opted for a full tungsten first wall in lieu of the original beryllium first wall design, beryllium remains an interesting first wall material for its low atomic number and being an excellent neutron multiplier. Its four-electron structure (Be I: $1s^2 2s^2$) introduces multi-electron correlations, doubly excited states, and dielectronic recombination processes, making the atomic kinetics more complex than those of lithium while remaining tractable in the fine-structure description, which provides the benchmark to assess the physics fidelity of the hybrid models in the present FCR code.

At $n_e = 10^{14} \text{ cm}^{-3}$, Fig. 7 shows that beryllium exhibits the most complex behavior among the three elements studied across all plasma properties. The radiative power loss displays a rich multi-peak structure, with primary, secondary, and tertiary maxima near 1–2 eV, 15–20 eV, and 30–40 eV, respectively. This structure arises from the sequential ionization from Be to Be^+ , Be^{2+} , Be^{3+} , and Be^{4+} , with each ionization stage contributing distinct spectroscopic features dominated by different atomic transitions.

The Hybrid- $(n_{\text{valence}} + 4)$ model reproduces this complex radiative structure with deviations below 15% across all temperature ranges and peaks. This level of accuracy is notable given the computational reduction achieved, as the number of levels decreases from nearly ten thousand in the fine-structure model to 413 in the extended hybrid model. The Hybrid- (n_{valence}) model fails to capture significant fine-structure contributions, with deviations of about 10% at the first radiative peak and increasing to approximately 30% and 100% at subsequent peaks, highlighting the importance of retaining fine-structure detail for higher-lying states in multi-electron systems.

The charge-state evolution exhibits four distinct ionization plateaus, each corresponding to a different beryllium ion. The transitions between these plateaus are sharper than those observed in lithium, reflecting more tightly bound electron configurations and steeper ionization potential gradients. The Hybrid- $(n_{\text{valence}} + 4)$ model accurately captures these ionization dynamics with deviations below 2% across the entire temperature range. The reduced hybrid model shows larger errors in critical transition regions, particularly during the Be^+ to Be^{2+} transition, where many-body effects dominate the population kinetics.

The accuracy trends are further confirmed by the parity plots in Fig. 8. The extended hybrid

model shows a tight clustering along the diagonal across all temperatures and densities, indicating close agreement with the fully fine-structure benchmark. The reduced hybrid model exhibits a noticeably broader scatter, reflecting the loss of important fine-structure selectivity when averaging begins too close to the ground configuration.

Beyond these accuracy considerations, an important advantage of the hybrid CR framework lies in its computational efficiency. In the case of beryllium, the reduction from 9,790 fine-structure levels to 413 levels in the extended hybrid model (Hybrid- $(n_{\text{valence}} + 4)$), and further down to 85 levels in the reduced version (Hybrid- (n_{valence})), directly lowers the computational effort required to solve the CR rate equations. Since the linear algebra step scales approximately as $\mathcal{O}(N^3)$, reducing the size of the system produces a substantial decrease in solver time.

Furthermore, an equally important gain arises in the construction of the rate matrix. All rate coefficients are generated from the underlying cross-sections of the relevant atomic processes by integrating over a Maxwellian electron distribution. The computational cost of this step grows rapidly with the number of available states, as the total number of transitions between states increases rapidly with the size of the set of states. Reducing the number of active states from nearly ten thousand to a few hundred thereby produces a corresponding decrease in the number of transitions that must be evaluated and assembled. This reduction leads to a significant decrease in the computational cost of rate-matrix generation across all plasma densities considered in this study.

A direct computational benchmark illustrates the magnitude of this improvement. For beryllium, the extended hybrid model provides an average reduction in the total computation time, including both rate-matrix construction and the linear-system solution, by approximately a factor of twenty-five across all the electron densities considered in this work. Comparable reductions are observed for the lithium and helium cases, with average computational improvements of roughly eighteen-fold and six-fold, respectively. These results demonstrate that the hybrid framework provides consistently large efficiency gains across multiple plasma species.

For heavier ions, the computational advantage of the hybrid framework is expected to be even more pronounced. Detailed fine-structure CR modeling for such species may involve hundreds of thousands of levels and an extremely large number of level-to-level transitions, making direct calculations increasingly impractical. The scalability demonstrated for helium, lithium, and beryllium therefore indicates that the hybrid approach is well suited for extending CR modeling to higher-Z impurities, where maintaining fine-structure fidelity, while managing computational cost, is essential for accurate plasma diagnostics and integrated fusion modeling.

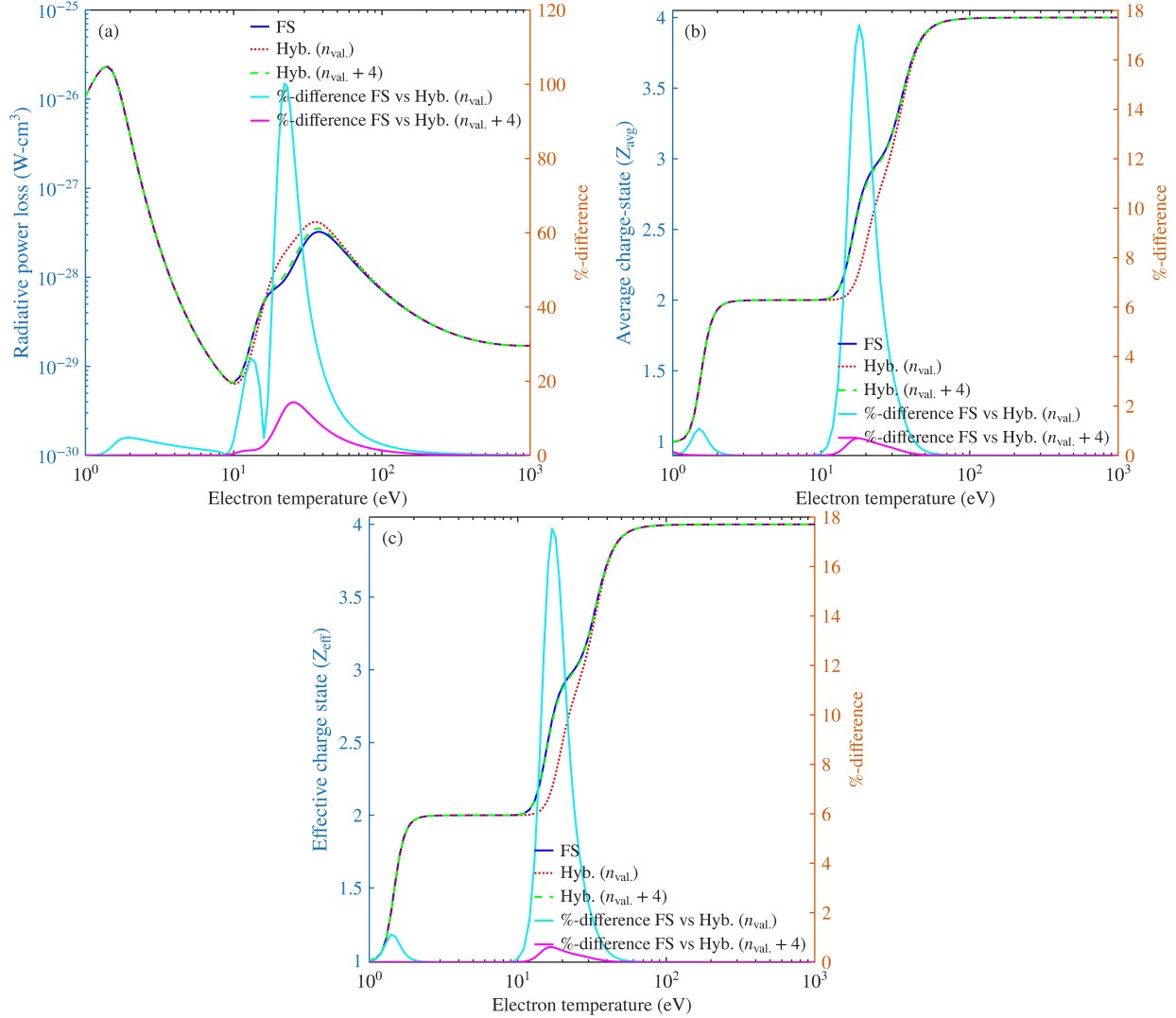


FIG. 7. **Beryllium:** Comparison of (a) radiative power loss, (b) average charge state, and (c) effective charge state obtained from the fine-structure CR model and two hybrid models, Hybrid- (n_{valence}) and Hybrid- $(n_{\text{valence}} + 4)$, at $n_e = 10^{14} \text{ cm}^{-3}$. Right-hand axes show the percentage deviation of each hybrid model from the fine-structure results. Here, "val." = valence and "Hyb." = Hybrid.

IV. CONCLUSION

In this work we have developed and benchmarked hybrid CR models that combine fine-structure resolution with superconfiguration averaging, offering a practical balance between accuracy and computational efficiency. We considered two variants, Hybrid- (n_{valence}) and Hybrid- $(n_{\text{valence}} + 4)$. The first model retains detailed fine-structure levels up to n_{valence} and the second up to $n_{\text{valence}} + 4$, whereas higher-lying states (up to $n = 10$) are statistically averaged into super-

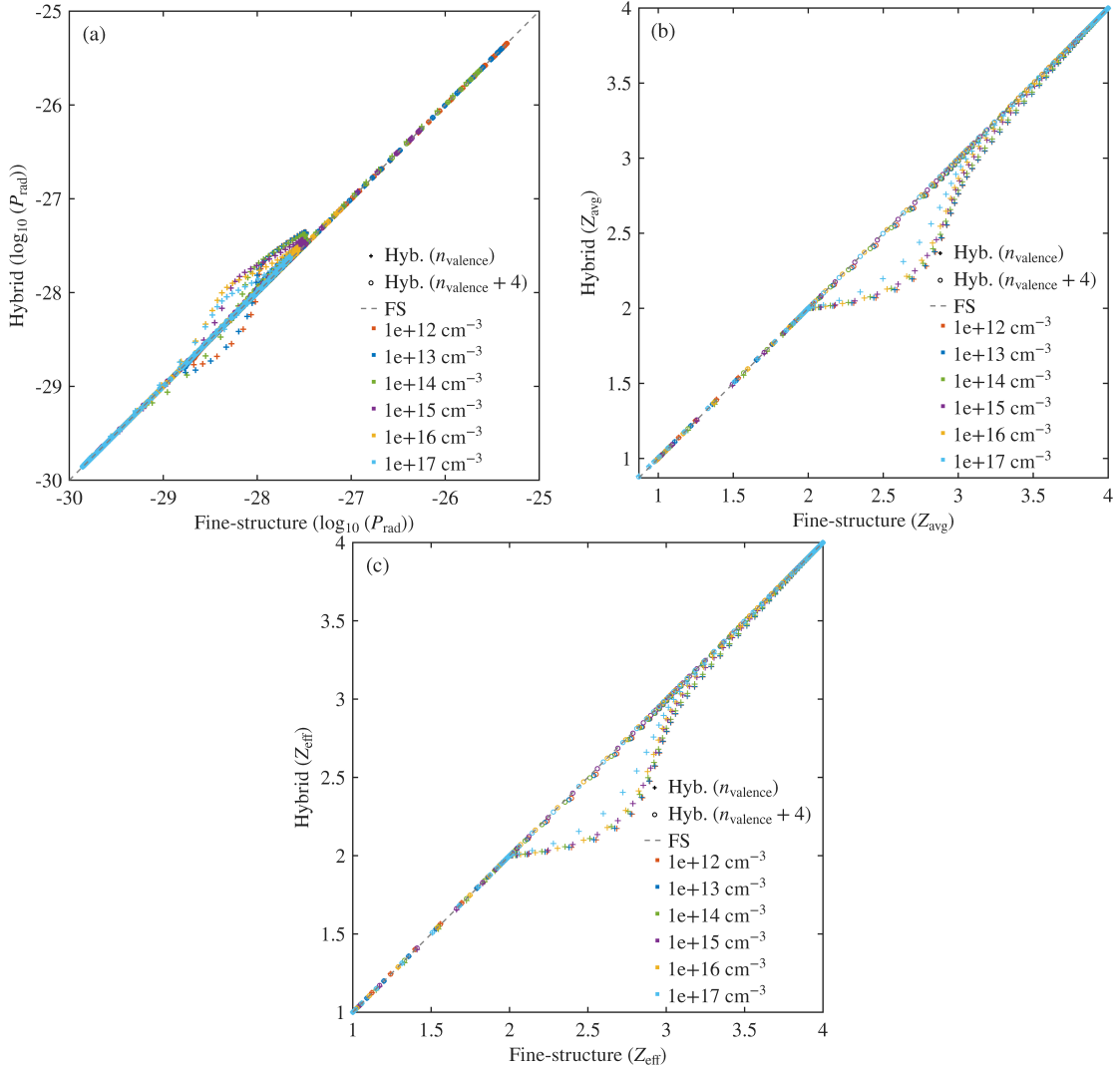


FIG. 8. Beryllium: Parity plots comparing (a) radiative power loss, P_{rad} , (b) average charge state, Z_{avg} , and (c) effective charge state, Z_{eff} , predicted by Hybrid- (n_{valence}) and Hybrid- $(n_{\text{valence}} + 4)$ models against the fine-structure CR model across electron densities from 10^{12} to 10^{17} cm^{-3} . The dashed diagonal represents perfect agreement ($y = x$); points closer to the line indicate better agreement with the fine-structure benchmark.

configuration states. Comparisons with fully fine-structure CR models for helium, lithium, and beryllium show that Hybrid- (n_{valence}) reproduces the overall trend of plasma observables, but introduces significant errors, particularly in radiation-dominated regimes, whereas Hybrid- $(n_{\text{valence}} + 4)$ shows much closer agreement with fine-structure benchmarks, with fewer errors and a significant reduction in computational cost compared to the full fine-structure model. These results establish the hybrid CR framework as a versatile and scalable strategy for plasma modeling, allowing users

to balance computational cost with the desired level of atomic-structure fidelity. The approach is well suited for fusion, astrophysical, and laboratory plasmas, where predictive accuracy must be maintained without additional computational overhead. Future studies will aim to extend and assess the hybrid approach for higher-Z ions and for non-Maxwellian electron distributions, thereby broadening its applicability to more complex plasma environments.

V. ACKNOWLEDGEMENTS

This work was jointly supported by the US Department of Energy through the Fusion Theory Program of the Office of Fusion Energy Sciences and the SciDAC partnership on Tokamak Disruption Simulation between the Office of Fusion Energy Sciences and the Office of Advanced Scientific Computing, at Los Alamos National Laboratory (LANL) under Contract No. 89233218CNA000001. C.J.F, M.C.Z, and J.C would like to specifically acknowledge Los Alamos National Laboratory (LANL) ASC PEM Atomic Physics Project. LANL is operated by Triad National Security, LLC, for the National Nuclear Security Administration of the US Department of Energy (Contract No. 89233218CNA000001). This research used resources of the National Energy Research Scientific Computing Center, a DOE Office of Science User Facility supported by the Office of Science of the U.S. Department of Energy under Contract No. DE-AC02-05CH11231 using NERSC award FES-ERCAP0032298.

REFERENCES

- ¹Y. Ralchenko, in *Modern Methods in Collisional-Radiative Modeling of Plasmas* (Springer, New York, 2016).
- ²D. Reiter, M. Baeva, O. Marchuk, and R. K. Janev, in *AIP Conference Proceedings* (American Institute of Physics, 2005), vol. 771, pp. 3–12.
- ³M. Goto and K. Sawada, *Journal of Quantitative Spectroscopy and Radiative Transfer* **137**, 23 (2014).
- ⁴I. Golovkin, J. MacFarlane, P. Woodruff, J. Bailey, G. Rochau, K. Peterson, T. Mehlhorn, and R. Mancini, *Journal of Quantitative Spectroscopy and Radiative Transfer* **99**, 199 (2006).
- ⁵H. A. Scott, in *Modern Methods in Collisional-Radiative Modeling of Plasmas* (Springer, 2016), pp. 81–104.

⁶A. K. Pradhan and S. N. Nahar, *Atomic astrophysics and spectroscopy* (Cambridge University Press, 2011).

⁷P. Greenland, Proceedings of the Royal Society of London. Series A: Mathematical, Physical and Engineering Sciences **457**, 1821 (2001).

⁸V. Donnelly, M. Malyshev, M. Schabel, A. Kornblit, W. Tai, I. Herman, and N. Fuller, Plasma Sources Science and Technology **11**, A26 (2002).

⁹H. Akatsuka, Advances in Physics: X **4**, 1592707 (2019).

¹⁰H.-K. Chung, M. H. Chen, W. L. Morgan, Y. Ralchenko, and R. W. Lee, High Energy Density Physics **1**, 3 (2005).

¹¹C. J. Fontes, J. Colgan, H. Zhang, and J. Abdallah Jr, Journal of Quantitative Spectroscopy and Radiative Transfer **99**, 175 (2006).

¹²S. Hansen, J. Bauche, C. Bauche-Arnoult, and M. Gu, High Energy Density Physics **3**, 109 (2007).

¹³C. J. Fontes, J. Colgan, and J. Abdallah Jr., in *Modern Methods in Collisional-Radiative Modeling of Plasmas*, p. 15, (Springer, New York, 2016).

¹⁴Z. Guo and X.-Z. Tang, Phys. Rev. Lett. **109**, 135005 (2012).

¹⁵X.-Z. Tang and Z. Guo, Physics of Plasmas **23**, 083503 (2016).

¹⁶Y. Zhang, J. Li, and X. Tang, Sci. Rep. **14**, 23448 (2024).

¹⁷H. Mao, Y. Zhang, and X. Tang, arXiv preprint arXiv:2311.09396 (2023).

¹⁸C. J. McDevitt, X.-Z. Tang, and Z. Guo, Physics of Plasmas **24**, 112702 (2017).

¹⁹C. J. McDevitt, Z. Guo, and X.-Z. Tang, Plasma Physics and Controlled Fusion **61**, 054008 (2019).

²⁰N. A. Garland, H.-K. Chung, C. J. Fontes, M. C. Zammit, J. Colgan, T. Elder, C. J. McDevitt, T. M. Wildey, and X.-Z. Tang, Physics of Plasmas **27**, 040702 (2020).

²¹D. Laurie, Mathematics of Computation **66**, 1133 (1997).

²²M. F. Gu, Canadian Journal of Physics **86**, 675 (2008).

²³Y.-K. Kim, Phys. Rev. A **64**, 032713 (2001).

²⁴V. Jonauskas, Atomic Data and Nuclear Data Tables **135**, 101363 (2020).

²⁵V. Jonauskas, Astronomy & Astrophysics **659**, A11 (2022).

²⁶K. Bartschat, Computer physics communications **114**, 168 (1998).

²⁷I. Bray, I. B. Abdurakhmanov, J. J. Bailey, A. W. Bray, D. V. Fursa, A. S. Kadyrov, C. M. Rawlins, J. S. Savage, A. T. Stelbovics, and M. C. Zammit, Journal of Physics B: Atomic,

Molecular and Optical Physics **50**, 202001 (2017).

²⁸C. J. Fontes, H. L. Zhang, J. Abdallah Jr, R. E. H. Clark, D. P. Kilcrease, J. Colgan, R. T. Cunningham, P. Hakel, N. H. Magee, and M. E. Sherrill, Journal of Physics B: Atomic, Molecular and Optical Physics **48**, 144014 (2015).

²⁹H. Summers and M. O'Mullane, *The Atomic Data and Analysis Structure* (Springer Berlin Heidelberg, Berlin, Heidelberg, 2005), pp. 399–413.

³⁰J. Abdallah Jr, M. E. Sherrill, D. P. Kilcrease, C. J. Fontes, H. Zhang, and J. Oelgoetz, High energy density physics **5**, 204 (2009).

³¹Y. V. Ralchenko and Y. Maron, Journal of Quantitative Spectroscopy and Radiative Transfer **71**, 609 (2001).

³²R. Clark and J. J. Abdallah, *Comparison calculations of radiated power loss for silicon and iron* (IAEA, 2003).

³³D. Layzer, Annals of Physics **8**, 271 (1959).

³⁴D. Reiter and S. Wiesen, Fusion Science and Technology **45**, 261–270 (2004).

³⁵R. Kaita, Plasma Physics and Controlled Fusion **61**, 113001 (2019).

³⁶S. Mirnov, Journal of Nuclear Materials **390-391**, 876 (2009).

³⁷M. Rubel, A. Widdowson, J. Grzonka, E. Fortuna-Zalesna, S. Moon, P. Petersson, N. Ashikawa, N. Asakura, D. Hamaguchi, Y. Hatano, et al., Fusion Engineering and Design **136**, 579–586 (2018).